A Second-Order Projection Method for Variable-Density Flows*

JOHN B. BELL AND DANIEL L. MARCUS

Lawrence Livermore National Laboratory, Livermore, California 94550

This paper describes a second-order projection method for variable-density incompressible flows. The method is suitable for both finite amplitude density variations and for fluids that are modeled using a Boussinesq approximation. It is based on a second-order fractional step scheme in which diffusion–convection terms are advanced without enforcing the incompressibility condition and the resulting intermediate velocity field is then projected onto the space of discretely divergence-free vector fields. The nonlinear convection terms are treated using a Godunov-type procedure that is second order for smooth flow and remain stable and non-oscillatory for nonsmooth flows with low fluid viscosities. The method is described for finite-amplitude density variation and the simplifications for a Boussinesq approximation are sketched. Numerical results are presented that validate the convergence properties of the method and demonstrate its performance on more realistic problems. © 1992 Academic Press, Inc.

1. INTRODUCTION

Flows in which spatial density variation plays an important role are ubiquitous in nature and technology. The generation of baroclinic vorticity by the interaction of non-parallel pressure and density gradients leads to a richness of structure and scale that presents a formidable computational challenge. Most work in this field has made use of the Boussinesq approximation, in which momentum effects due to density variation are ignored, and the temperature dependence on the density is accounted for via a linearized forcing term coupling the energy and momentum equations. This is a small amplitude approximation, however, and it introduces a symmetry to the equations that is non-physical. The method described herein uses no such approximation. In this paper we develop a high-resolution computational tool for solving the full, variable density Navier–Stokes equations. The method is a straightforward extension of the second-order projection method developed

by Bell *et al.* [1] (hereafter referred to as BCG) for the incompressible Navier–Stokes equations. BCG is a higher-order extension of Chorin's projection algorithm [2], based on a discrete form of the Hodge decomposition, which states that a vector field V defined on a region Ω can be decomposed into the gradient of a scalar potential ϕ and a divergence-free component V^d, subject to some type of boundary condition.

In its most basic form, the projection method requires the solution of advection–diffusion equations, which are then projected onto the space of divergence-free vector fields. The projection exploits the orthogonality of the pressure gradient with divergence-free velocity fields that is manifest in the Hodge decomposition and, in BCG, is accomplished via a discrete-Galerkin finite difference formulation using a local basis for discretely divergence-free vector fields developed by Stephens *et al.* [3] and Solomon and Szymczak [4] for the steady Navier–Stokes equations. (Equivalently, the incompressibility constraint can be enforced by computing the gradient component and subtracting it from the intermediate solution to the advection–diffusion equations). BCG extends the algorithm to higher order by introducing more coupling between the advection–diffusion step and the projection and by incorporating a variant of the unsplit second-order Godunov methodology developed by Colella [5] for inviscid, compressible flows into the evaluation of the nonlinear advection terms in the momentum equations. This provides a temporal discretization that is second order for smooth flows and stable in regions with steep gradients, even for singular initial data and in the limit of vanishing viscosity. These properties make the method extremely well suited for application to strongly-forced buoyancy-driven flows which are characterized by fine structure and a wide range of length scales.

In this paper, we consider only the two-dimensional case; the ideas and methodologies can be easily extended to three-dimensional problems. In the next section we describe the method, reviewing the key ideas in BCG and stressing those elements that characterize its extension to variable-density flows. In Section 3, in order to validate the second-order accuracy of the method, we study a model problem in a

square cavity with smooth initial data. In Section 4, examples are presented that serve to illustrate the wide range of applicability of the method. Calculations are carried out in planar and axisymmetric geometries, for both Boussinesq and "real" variable density flows.

2. DESCRIPTION OF THE METHOD

We solve the incompressible Navier–Stokes equations for flows with finite-amplitude density variation. Conservation of mass is described by an advection equation. The equations take the form

$$U_t + (U \cdot \nabla)U = \frac{1}{\rho}(LU - \nabla p + F) \tag{2.1}$$

$$\rho_t + (U \cdot \nabla)\rho = 0 \tag{2.2}$$

$$\nabla \cdot U = 0, \tag{2.3}$$

where $U = \binom{u}{v}$ is the velocity vector, ρ is the density, p is the pressure, and F is a forcing term. Here, the operator L, defined by

$$LU = \nabla \cdot \mu(\nabla U + (\nabla U)^T),$$

represents the viscous terms where μ is the viscosity of the fluid which we allow to depend on density.

2.1. Basic Methodology

Our strategy for solving the system (2.1)–(2.3) is a fractional step scheme having two parts: first we solve the advection–diffusion equations (2.1)–(2.2) without strictly enforcing the incompressibility constraint, then, we project the resulting velocity field onto the space of discretely divergence-free vector fields. The algorithm will only be sketched here for a uniform spatial grid; the reader is referred to [1, 6] for a more detailed description. For the diffusion–convection step we solve for the intermediate velocity and the new density field using

$$\frac{U^* - U^n}{\Delta t} + [(U \cdot \nabla)U]^{n + 1/2}$$

$$= \frac{1}{\rho^{n+1/2}} \left[L^h \left(\frac{U^n + U^*}{2} \right) - \nabla p^{n-1/2} + \frac{F^n + F^{n+1}}{2} \right] \tag{2.4}$$

$$\frac{\rho^{n+1} - \rho^n}{\Delta t} + [(U \cdot \nabla)\rho]^{n+1/2} = 0, \tag{2.5}$$

where L^h is a standard finite-difference approximation to the L and $\rho^{n+1/2}$ on the right-hand side of (2.4) is the average of ρ^n and ρ^{n+1}. The pressure gradient is evaluated at $t^{n-1/2}$ and is treated as a source term in (2.4). (The pressure gradient is only computed at the 1/2-time levels.)

The advection terms in (2.4)–(2.5), namely $(U \cdot \nabla)U$ and $(U \cdot \nabla)\rho$, are approximated at time $t^{n+1/2}$ to second-order in space and time using an explicit predictor–corrector scheme. This scheme uses only the available data at t^n; thus, the implicit part of (2.4)–(2.5) corresponds to two decoupled heat equation solvers.

The convection algorithm is a second-order upwind method based on ideas first introduced by Colella [5]. The discretization is based on a staggered grid system indicated in Fig. 1. Here, U, ρ, and ∇p are given at the primary grid points denoted by a $\bullet$. Other quantities, such as $\nabla \cdot U$, p, and a stream function, ψ, will be defined on the dual grid points denoted by a $\times$. Typically, the primary grid points will lie on the boundary of the domain for imposing viscous boundary conditions; however, in axisymmetric coordinates we stagger the grid and use reflection symmetry at the boundary. In the predictor we extrapolate the velocity and density to the cell edges of the dual grid at $t^{n+1/2}$ using a second-order Taylor series expansion. For edge-$i + 1/2, j$ this gives

$$U_{i+1/2,j}^{n+1/2,L} = U_{ij}^n + \frac{\Delta x}{2} U_{x,ij}^n + \frac{\Delta t}{2} U_{t,ij}^n$$

$$\rho_{i+1/2,j}^{n+1/2,L} = \rho_{ij}^n + \frac{\Delta x}{2} \rho_{x,ij}^n + \frac{\Delta t}{2} \rho_{t,ij}^n$$

when extrapolating from i, j and

$$U_{i+1/2,j}^{n+1/2,R} = U_{i+1,j}^n - \frac{\Delta x}{2} U_{x,i+1,j}^n + \frac{\Delta t}{2} U_{t,i+1,j}^n$$

$$\rho_{i+1/2,j}^{n+1/2,R} = \rho_{i+1,j}^n - \frac{\Delta x}{2} \rho_{x,i+1,j}^n + \frac{\Delta t}{2} \rho_{t,i+1,j}^n$$
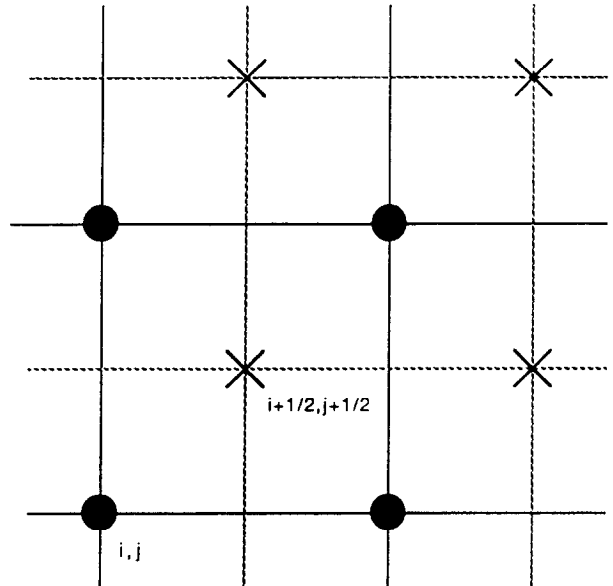

FIG. 1. Staggered grid system. U, ρ, and ∇p are defined at i, j; $\nabla \cdot U$, p, and ψ are defined at $i + \frac{1}{2}, j + \frac{1}{2}$.

when extrapolating from $i + 1, j$ with analogous formulae for the other edges. The differential equations (2.1) and (2.2) are then used to eliminate the time derivatives to obtain

$$U_{i+1/2,j}^{n+1/2,L} = U_{ij}^n + \left(\frac{\Delta x}{2} - u\frac{\Delta t}{2}\right)U_{x,ij}^n - \frac{\Delta t}{2}vU_{y,ij}$$

$$+ \frac{\Delta t}{2}\frac{1}{\rho_{ij}^n}(L^h U_{ij}^n - \nabla p_{ij}^{n-1/2} + F_{ij}^n) \quad (2.6a)$$

$$\rho_{i+1/2,j}^{n+1/2,L} = \rho_{ij}^n + \left(\frac{\Delta x}{2} - u\frac{\Delta t}{2}\right)\rho_{x,ij}^n - \frac{\Delta t}{2}v\rho_{y,ij} \quad (2.6b)$$

$$U_{i+1/2,j}^{n+1/2,R} = U_{i+1,j}^n - \left(\frac{\Delta x}{2} + u\frac{\Delta t}{2}\right)U_{x,i+1,j}^n$$

$$- \frac{\Delta t}{2}vU_{y,i+1,j} + \frac{\Delta t}{2}\frac{1}{\rho_{i+1,j}^n}$$

$$\times (L^h U_{i+1,j}^n - \nabla p_{i+1,j}^{n-1/2} + F_{i+1,j}^n) \quad (2.6c)$$

$$\rho_{i+1/2,j}^{n+1/2,L} = \rho_{i+1,j}^n - \left(\frac{\Delta x}{2} + u\frac{\Delta t}{2}\right)\rho_{x,i+1,j}^n$$

$$- \frac{\Delta t}{2}v\rho_{y,i+1,j}. \quad (2.6d)$$

Equation (2.6) represents the final form of the predictor. In evaluating these terms the first-order derivatives normal to the edge (in this case U_x and ρ_x) are evaluated using a monotonicity-limited centered difference slope approximation; the transverse derivative terms (U_y and ρ_y) are evaluated using an upwind difference.

In the corrector we first resolve the ambiguity in the edges values. The convective part of (2.1) corresponding to the velocity normal to the edge is of the form $u_t + uu_x = source$ terms. This suggests the following upwind determination of the normal velocity component:

$$u_{i+1/2,j} = \begin{cases} u^L & \text{if } u^L \geqslant 0, u^L + u^R \geqslant 0 \\ 0 & \text{if } u^L < 0, u^R > 0 \\ u^R & \text{otherwise.} \end{cases} \quad (2.7)$$

(We suppress the $i + 1/2, j$ spatial indices on left and right states here and in the next equation.) We now upwind ρ and U based on $u_{i+1/2,j}$:

$$U_{i+1/2,j}, \rho_{i+1/2,j}$$

$$= \begin{cases} U^L, \rho^L & \text{if } u_{i+1/2,j} > 0 \\ U^R, \rho^R & \text{if } u_{i+1/2,j} < 0 \\ 1/2(U^L + U^R), 1/2(\rho^L + \rho^R) & \text{if } u_{i+1/2,j} = 0. \end{cases} \quad (2.8)$$

Finally, we use these upwind values to form an approximation to the convective derivates in (2.1) and (2.2)

$$uU_x + vU_y \approx \frac{1}{2}(u_{i+1/2,j} + u_{i-1/2,j})\frac{(U_{i+1/2,j} - U_{i-1/2,j})}{\Delta x}$$

$$+ \frac{1}{2}(v_{i,j+1/2} + v_{i,j-1/2})\frac{(U_{i,j+1/2} - U_{i,j-1/2})}{\Delta y}$$

$$\quad (2.9a)$$

$$u\rho_x + v\rho_y \approx \frac{1}{2}(u_{i+1/2,j} + u_{i-1/2,j})\frac{(\rho_{i+1/2,j} - \rho_{i-1/2,j})}{\Delta x}$$

$$+ \frac{1}{2}(v_{i,j+1/2} + v_{i,j-1/2})\frac{(\rho_{i,j+1/2} - \rho_{i,j-1/2})}{\Delta y}.$$

$$\quad (2.9b)$$

The velocity field computed in the first step is not, in general, divergence-free. The projection step of the algorithm decomposes the result of the first step into a discrete gradient of a scalar potential and a discretely divergence-free vector field which correspond, respectively, to the new approximation to the pressure gradient and an update for the velocity. In particular, if $\mathbf{P}$ represents the projection then

$$\frac{U^{n+1} - U^n}{\Delta t} = \mathbf{P}\left(\frac{U^* - U^n}{\Delta t} + \frac{1}{\rho^{n+1/2}}\nabla p^{n-1/2}\right) \quad (2.10a)$$

$$\frac{1}{\rho^{n+1/2}}\nabla p^{n+1/2} = (\mathbf{I} - \mathbf{P})\left(\frac{U^* - U^n}{\Delta t} + \frac{1}{\rho^{n+1/2}}\nabla p^{n-1/2}\right).$$

$$\quad (2.10b)$$

(Note that the vector field we project is not U^*; it is an approximation to $U_t + \rho^{-1}\nabla p$. This distinction is important in formulating the outflow boundary conditions.) The vector field decomposition described by (2.10) can be cast into the framework of the more conventional projection (see [1]) by changing from the standard inner product to a ρ-based inner product. In particular, we define the inner product of two vector fields V_1 and V_2 to be

$$\iint V_1 \cdot V_2 \rho \, dm,$$

where dm is a volume measure ($dx\,dy$ in Cartesian coordinates and $r\,dr\,dz$ in axisymmetric coordinates). In this inner product, divergence-free vector fields with zero normal components are orthogonal to vector fields of the form $\rho^{-1}\nabla\phi$. Consequently, the projection for variable density flow is simply the standard projection with respect to a density-weighted inner product.

To define the discrete approximation of the projection we

must first define discrete divergence and gradient operators and a discrete ρ-weighted inner product. We have used

$$(DU)_{i+1/2,\,j+1/2}$$

$$\equiv \frac{1}{2\xi_{i+1/2,\,j+1/2}}$$

$$\times \left[\frac{\begin{pmatrix} (\xi_{i+1,\,j+1}u_{i+1,\,j+1} - \xi_{i,\,j+1}u_{i,\,j+1}) \\ + (\xi_{i+1,\,j}u_{i+1,\,j} - \xi_{ij}u_{ij}) \end{pmatrix}}{\Delta x} \right.$$

$$\left. + \xi_{i+1/2,\,j+1/2} \frac{\begin{pmatrix} v_{i+1/2,\,j+1/2} - v_{i+1,\,j}) \\ + (v_{i,\,j+1} - v_{ij}) \end{pmatrix}}{\Delta y} \right] \quad (2.11\text{a})$$

for divergence,

$$(G\phi)_{ij} = \frac{1}{2} \left[\frac{\begin{pmatrix} \phi_{i+1/2,\,j+1/2} - \phi_{i-1/2,\,j+1/2} \\ + \phi_{i+1/2,\,j-1/2} - \phi_{i-1/2,\,j-1/2} \end{pmatrix}}{\Delta x} \right. \left. \frac{\begin{pmatrix} \phi_{i+1/2,\,j+1/2} - \phi_{i+1/2,\,j-1/2} \\ + \phi_{i-1/2,\,j+1/2} - \phi_{i-1/2,\,j-1/2} \end{pmatrix}}{\Delta y} \right] \quad (2.11\text{b})$$

for the gradient, and

$$(V_1, V_2)_\rho \equiv \sum\sum V_{1,\,ij} \cdot V_{2,\,ij}\rho_{ij}\xi_{ij}$$

for the inner product. Here ξ_{ij} is a metric coefficient defined by

$$\xi_{ij} = \begin{cases} 1 & \text{for Cartesian coordinates} \\ x_{ij} & \text{for axisymmetric coordinates.} \end{cases}$$

Note that the divergence operator defines the divergence at the zone centers $(i+1/2, j+1/2)$ (denoted $\times$ in Fig. 1) in terms of the velocities at the neighboring corners; the gradient uses scalar data at zone centers to compute gradients at grid points. This choice of the discretization corresponds to the bilinear velocity and piecewise constant pressure finite element basis of Fortin [7]. With these definitions of D and G, the discrete operators are skew adjoint, i.e., $G = -D^T$, and satisfy a discrete analog of integration by parts

$$(U, \rho^{-1}G\phi)_\rho = \sum\sum U_{ij} \cdot (\rho^{-1}G\phi)_{ij}\,\rho_{ij}\xi_{ij}$$

$$= -\sum\sum (DU)_{i+1/2,\,j+1/2}\phi_{i+1/2,\,j+1/2}$$

$$\times \xi_{i+1/2,\,j+1/2} + \text{boundary terms.} \quad (2.12)$$

Equation (2.12) shows that discretely divergence-free vector

fields are orthogonal to vector fields of the form $\rho^{-1}G\phi$ (subject to suitable boundary conditions); consequently, we can define a discrete projection so that any discrete vector field can be uniquely decomposed into the discrete gradient divided by density (as defined by (2.11)) and a component in the null space of D.

Several approaches are possible for computing this decomposition. We have used the discrete Galerkin approach first introduced by Stephens et al. [3]. This approach is based on the observation that the local vector fields defined by

$$S_{ij}^{k+1/2,\,l+1/2} = \begin{cases} \xi_{ij}^{-1}((-1)^{l-j}, (-1)^{k-i+1}) \\ \quad \text{for} \quad i=k, k+1; j=l, l+1 \\ (0, 0) \quad \text{for all other} \quad i, j \end{cases}$$

from a local basis for the kernel of D so that any divergence-free vector field, in particular, $(U^{n+1} - U^n)/\Delta t$, can be written as

$$\frac{U^{n+1} - U^n}{\Delta t} = \sum \psi_{i+1/2,\,j+1/2} S^{i+1/2,\,j+1/2}.$$

The coefficients in the expansion can be determined from the Galerkin projection

$$\sum \psi_{i+1/2,\,j+1/2} (S^{i+1/2,\,j+1/2}, S^{k+1/2,\,l+1/2})_\rho$$

$$= \left(\frac{U^* - U^n}{\Delta t} + \nabla p^{n-1/2}, S^{k+1/2,\,l+1/2} \right)_\rho. \quad (2.13)$$

The system of equations defined by (2.13) is symmetric and positive-definite with spectral properties equivalent to discretizations of the elliptic operator $\nabla \cdot \rho\nabla$. In fact, the S's correspond to discrete curls; hence (2.13) corresponds to a discrete stream-function vorticity equation (except that the right-hand side is the angular momentum rather than the vorticity). We solve the system by means of a conjugate-gradient algorithm preconditioned with a modified incomplete Cholesky factorization.

2.2. Outflow Boundary Conditions

There are two basic components to the outflow boundary treatment. For the first step of the algorithm, namely, the diffusion–convection step, the density and velocity fields are simply extrapolated beyond the outflow edge. This has the effect of characteristic outflow for the convection with a natural boundary condition for the diffusion. The treatment of outflow in the projection requires more care. The choice of the outflow boundary condition in the projection has the effect of completing the specification of the Hodge decomposition. Our basic approach is to use a "natural" boundary condition in the projection as discussed by Bell et al. [6]

with a modification to weakly impose hydrostatic equilibrium at the outflow.

The boundary condition can be derived by focusing on either the gradient component or the divergencefree component of the vector field; we will use the latter because it more closely reflects the discrete-Galerkin method. We introduce a stream function ψ such that $(U^{n+1} - U^n)/\Delta t = \nabla \times \psi$, where ψ explicitly satisfies the computable boundary conditions on Dirichlet boundaries. To motivate the boundary condition treatment we first consider the projection without a boundary correction at the outflow. In this case the projection is defined by requiring

$$\iint (\nabla \times \psi) \cdot (\nabla \times \chi) \rho \, dm = \iint V \cdot (\nabla \times \chi) \rho \, dm \quad (2.14)$$

for all χ that vanish on the Dirichlet boundaries. (Equation (2.14) is the continuous analog of (2.13), where the curl terms correspond to the Ψ's.) If we integrate (2.14) by parts and rearrange terms we obtain

$$\iint [\nabla \cdot (\rho \nabla \psi) + (\nabla \times \rho V)] \chi \, dm$$

$$= \int_0 \left(\frac{\partial \psi}{\partial \mathbf{n}} + V \cdot \mathbf{t} \right) \chi \rho \, dS$$

or

$$-\nabla \cdot (\rho \nabla \psi) = \nabla \times \rho V$$

with

$$\frac{\partial \psi}{\partial \mathbf{n}} = -V \cdot \mathbf{t}$$

on the outflow boundary, where $\mathbf{t}$ is the unit tangent at the boundary. From the definition of V in (2.10) we see that (2.14) weakly associates the tangential component of V with the update for the tangential velocity or, equivalently, weakly enforces $\partial p / \partial t = 0$ on the outflow face. However, from Eq. (2.4) $V \approx \rho^{-1}(LU - (U \cdot \nabla) U + F)$ which, near an outflow boundary, is typically dominated by F, particularly for strongly forced problems. Thus, (2.14) leads to a large acceleration term for the tangential velocity at an outflow boundary. This difficulty arises because the force should be balanced by the pressure gradient; i.e., at the outflow we want to enforce

$$\frac{\partial p}{\partial t} = F \cdot \mathbf{t}$$

which effectively says that the fluid exiting the domain is in

hydrostatic equilibrium. To weakly impose this condition to the right-hand side of (2.14) we add the integral correction

$$\int_{\hat{o}} F \cdot \mathbf{t} \, dS.$$

2.3. Time Step Strategy

Since the Godunov scheme is explicit, a CFL condition must be satisfied in order to ensure stability. However, in many situations, such as having the fluids initially at rest, the gravitational forcing term is sufficiently stiff to require a more restrictive time step than a standard CFL estimate would predict. We have augmented the standard CFL estimate by setting

$$\Delta t^{n+1} = c \min \left[\left(\frac{2 \min(\Delta x, \Delta y)}{|\nabla p_{ij} - F_{ij}|} \right)^{1/2}, \frac{\Delta x_{ij}}{|u_{ij}^n|}, \frac{\Delta y_{ij}}{|v_{ij}^n|} \right] \quad (2.15)$$

with the additional constraint that $\Delta t^{n+1} \leqslant 1.1 \, \Delta t^n$. The constant, c, is a safety factor to be determined experimentally. In all of the computations described in Section 4 we have taken $c = 1/2$.

2.4. Boussinesq Flows

A broad range of variable density flows have small density variations that can be modeled using a Boussinesq approximation. In the Boussinesq approximation density variations are assumed to be sufficiently small so that the density variation can be ignored in the momentum equation. The equations are only coupled through a gravitational forcing term. With these approximations the equations reduce to

$$U_t + (U \cdot \nabla) U = -\nabla p + \varepsilon \, \Delta U + \gamma \hat{\jmath} \theta \quad (2.16)$$

$$\theta_t + (U \cdot \nabla) \theta = \kappa \, \Delta \theta \quad (2.17)$$

$$\nabla \cdot U = 0, \quad (2.18)$$

where θ is the temperature. In these equations ε, κ, and γ are the kinematic viscosity, thermal diffusivity, and a gravitational constant that incorporates the coefficient of volume expansion, and $\hat{\jmath}$ is the unit vector in the vertical direction. (See Chandrasekhar [8] for a detailed discussion of the Boussinesq approximation.) When the equations are suitably nondimensionalized these parameters collapse into the dimensionless groups appropriate to the particular flow regime.

The methodology presented above can be directly applied to the Boussinesq equations by removing the density weighting in the projection and accounting for thermal diffusion in (2.17).

TABLE I

Convergence Results—Velocity

Case	32–64	Rate	64–128	Rate	128–256
Euler	2.819e-03	2.27	5.845e-04	2.22	1.256e-04
$R = 100$	7.886e-04	1.95	2.044e-04	1.88	5.539e-05

3. CONVERGENCE STUDY

In this section, results are given that demonstrate the rate of convergence of the method discussed in the previous section. For this purpose, we define a smooth initial stream function and density field inside the unit square:

$$\psi^0(x, y) = \pi^{-1} \sin^2(\pi y) \sin^2(\pi x) \tag{3.1}$$

$$\rho^0(y) = 1 - \tfrac{1}{2}\tanh(y - \tfrac{1}{2}), \tag{3.2}$$

where the initial velocities $u(x, y)$ and $v(x, y)$ are given, in the usual way, by $u = \partial\psi/\partial y$ and $v = -\partial\psi/\partial x$. The velocity satisfies homogeneous Dirichlet boundary conditions; boundary conditions on the density are determined by second-order extrapolation from the outermost interior cells. For the purposes of this convergence study, the body force term was omitted from the momentum equations.

We will consider two specific cases: inviscid flow (the incompressible Euler equations) and a viscous case with a Reynolds number of 100. For each case, the solution is computed on uniform grids, $\Delta x = \Delta y = 1/2^n$ for 2^n time steps, for $n = 4, 5, ..., 7$. For the purpose of establishing a convergence rate, a uniform time step is desired. In each of the three cases we set $\Delta t = 1/2\, \Delta x$ which gives an effective CFL of 0.5. We measure the difference in both the density and velocity for grids of adjacent resolution. In the viscous case, we measure pointwise differences summed (l^2) over points where coarse and fine grids coincide. In our formulation of the method for the Euler equations a staggered grid is used; hence, we compare the coarse grid answer with the average of the fine grid cells covering it. In either case, the l^2 norm of these differences is proportional to the error on the coarser grid and is used to compute the numerical convergence rates. The results for velocity and density are summarized in the Tables I and II.

TABLE II

Convergence Results—Density

Case	32–64	Rate	64–128	Rate	128–256
Euler	5.855e-04	2.37	1.132-04	2.34	2.230e-05
$R = 100$	3.926e-04	2.23	8.330-05	2.21	1.795-05

Second-order accuracy is apparent for velocity and density fields in the Euler case and for the density field for the $R = 100$ case. We observe a slight deterioration in accuracy in the velocity in the $R = 100$ case. A more detailed analysis of the error indicates that the regions of high error are clustered in irregular blotches in the interior of the domain, suggesting that the deterioration is most likely related to limiting effects.

4. EXAMPLES

To illustrate the performance of the method on problems modeled under the Boussinesq approximation, we consider the evolution of an axisymmetric thermal at high Rayleigh number and two-dimensional channel flow past a heated strip. As examples of flows with finite-amplitude density variation, we show the evolution of both single and complex modes of a Rayleigh–Taylor instability and the interaction of an axisymmetric vortex ring with a density interface.

4.1. Axisymmetric Thermal

A thermal is a region of self-convecting buoyant fluid which, as it moves, deforms due to vorticity generated by the interaction between the gravitational pressure gradient and the density gradient at the interface with the surrounding fluid. This can be observed, for example, in the formation of cumulus clouds [9], in the flow that results when a volume of fluid is heated by a sudden release of energy [10], or at the onset of motion in Rayleigh–Benard convection, in which thermals are ejected from the conduction layer into the surrounding fluid [11].

Numerical simulations of thermals have been carried out by several investigators (e.g., Anderson [12]), but these have been limited to relatively early times and Cartesian geometry.

The initial data are zero velocity everywhere, and

$$\theta(r, z, 0) = \theta_0(r, z) = \frac{1}{2}\left[1 + \tanh\left(\frac{r - r_0}{\delta}\right)\right], \tag{4.1}$$

which represents a sphere of hot fluid in cold surroundings. The interface has been desingularized to minimize grid effects. Homogeneous Dirichlet boundary conditions and axial symmetry were imposed.

For this calculation, the Grashof number, defined as $Gr = g\beta d^3\delta\theta/\kappa^2$, is 8×10^9, and the Prandtl number, $Pr = \varepsilon/\kappa$, is 0.71, where κ is the thermal diffusivity, v is the kinematic viscosity, d is the initial diameter of the hot sphere, $\delta\theta$ is the scale of temperature variation, β is the thermal expansion coefficient, and g is the acceleration due to gravity. The calculations are carried out on a 200×600 grid. Numerical experiments have shown that the evolution of
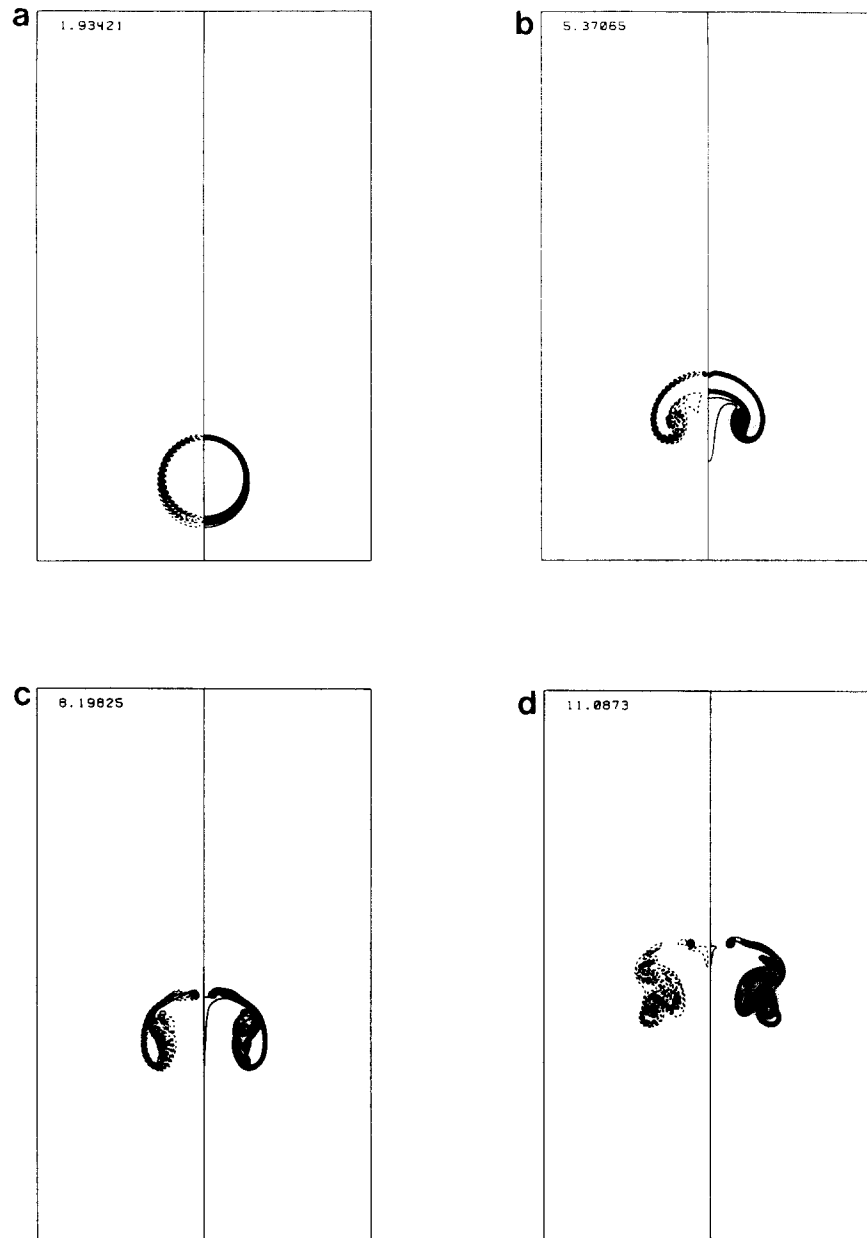
FIG. 2. (a)–(d) Axisymmetric thermal. Vorticity contours are shown on the left, temperature contours on the right. Grashof number = 8×10^9, Prandtl number = 0.71.

the flow is relatively insensitive to boundary effects except for the generation of thin boundary layers at the edge of the domain due to the "no-slip" condition there. We have plotted only the interior of the computational domain to suppress the plotting of these boundary layers. Results are shown in Figs. 2a–h. The left half-plane shows vorticity contours; temperature contours are shown on the right.

In the first frame, we see that the effect of baroclinicity is to create a vortex sheet at the interface between hot and cold fluids. Next, the vortex sheet curls up, causing the mass of

hot fluid to assume its characteristic mushroom shape. At the crown of the thermal, a small ringlet of countersign vorticity is observed, "notching" the temperature contours and signifying the onset of a topological change in the main body of the thermal from a mushroom to a ring configuration. A thermal wake trails the main mass of hot fluid. In the next frame, most of the hot fluid has been pulled into the shoulders of the thermal. The crown has separated, resulting in a layering of opposite-signed vorticity across the interface, and there is a large countersign vortical structure in the
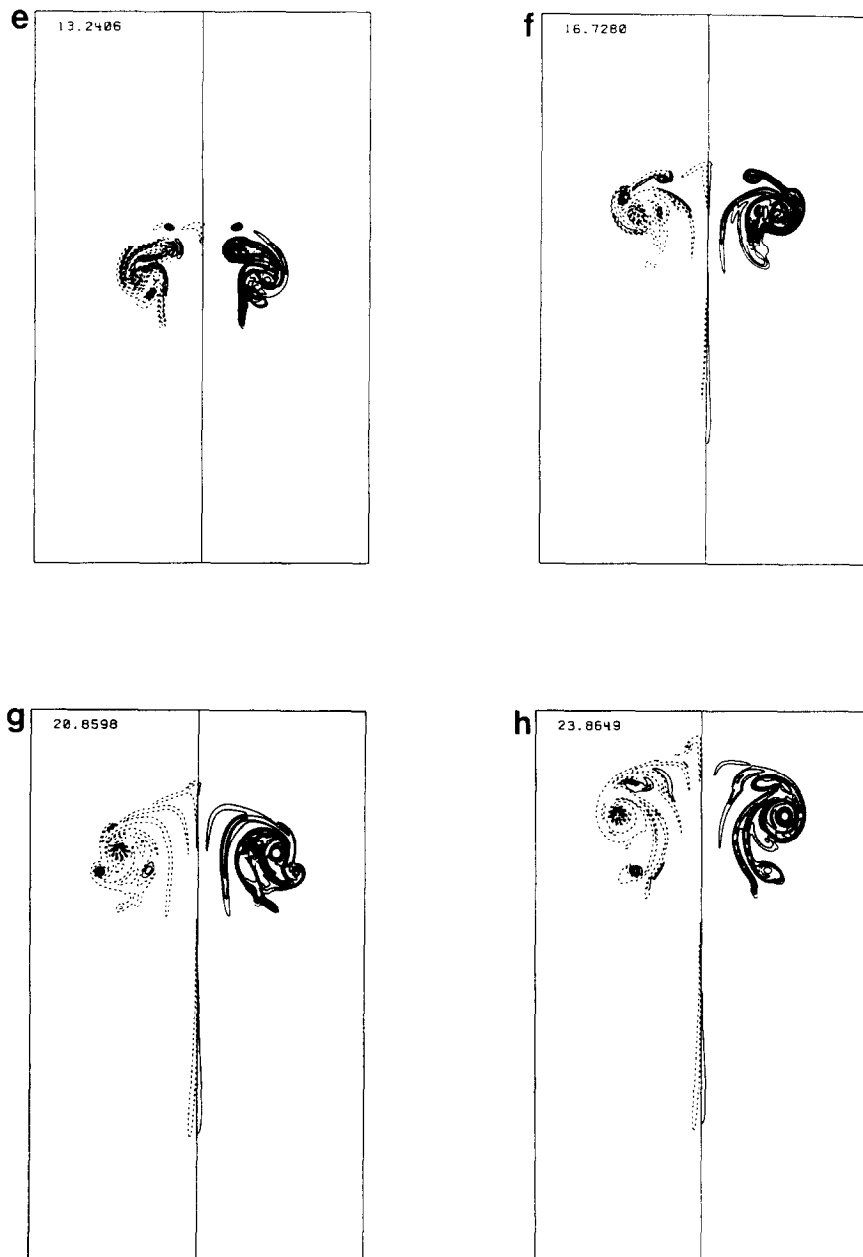
FIG. 2. (e)-(h) Axisymmetric thermal (continued). Vorticity contours are shown on the left, temperature contours on the right. Grashof number 8×10^9, Prandtl number = 0.71.

core. The next two frames show the crown separating further with the expansion of the vortex ringlet at the top and convective mixing in the core manifest as folding of the temperature and vorticity contours. Discrete vortices of both signs are observed in the core. In the last three frames, the thermal continues to rise and expand due to the entrainment of the surrounding fluid. The ringlet at the top has been absorbed, and wispy spiral arms are thrown out from the main body. There are still several persistent vortices of both signs in the core, and a thermal wake several diameters

long trails the thermal. A more detailed study of this flow has been undertaken [13].

4.2. Two-Dimensional Poiseuille Flow Past a Heated Strip

This configuration can be regarded as an idealized model of the fluid mechanics associated with a chemical vapor deposition reactor. Reactants are passed over a substrate heated to a temperature at which a desired chemical reaction will occur, and products are deposited in a thin
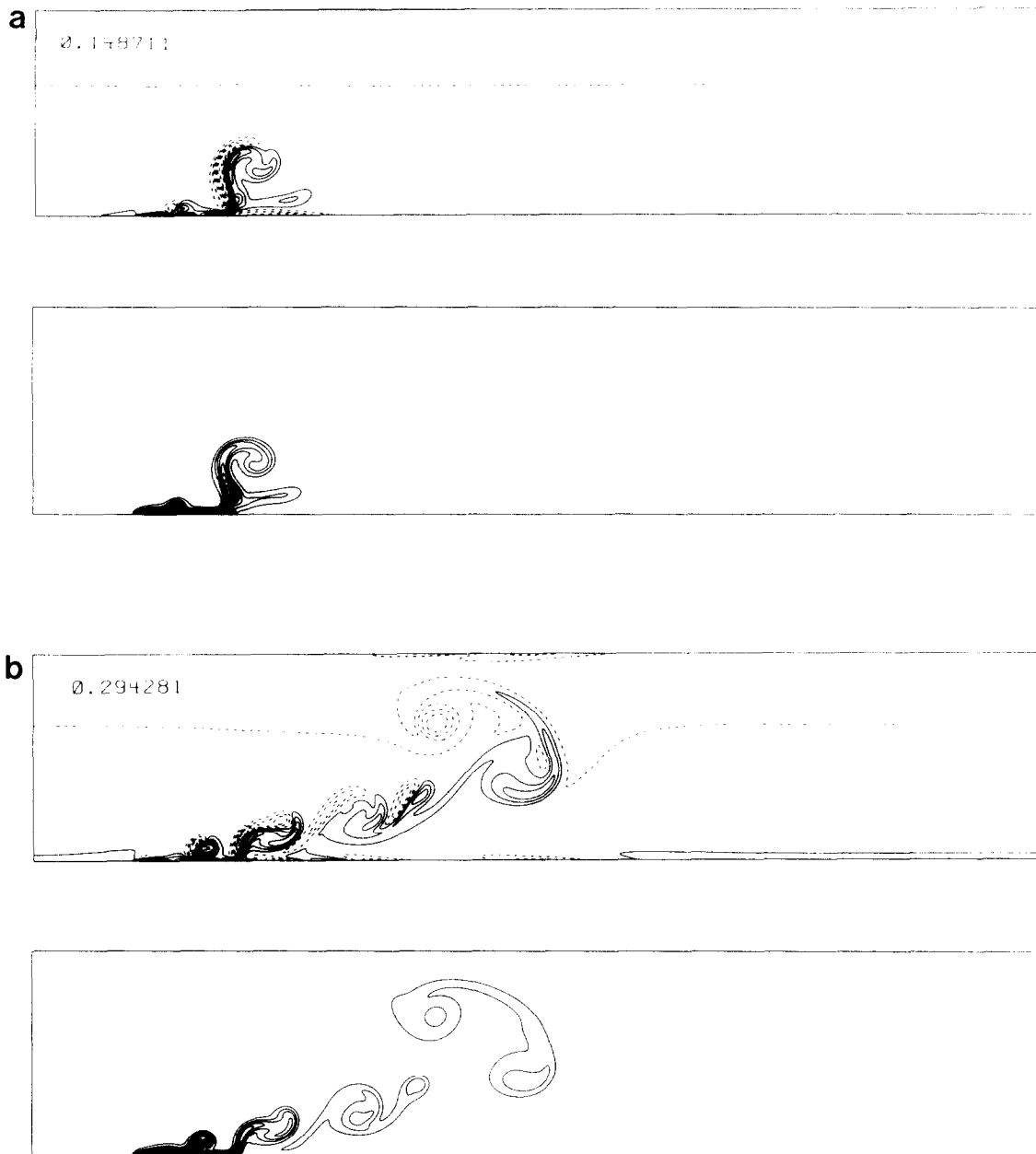
a

0.14871

b

0.294281

FIG. 3. (a)-(b) Poiseuille flow past a heated strip. Vorticity contours above, temperature contours below. Reynolds number = 50, Peclet number = 7.5, Richardson number = 750.

layer on the substrate. An understanding of the thermal and fluid transport properties of this system is essential to the development of a consistent process.

The imposition of an external velocity scale U introduces an additional dimensionless group into the specification of the problem. If Eqs. (2.16)-(2.18) are nondimensionalized by the inertial time d/U, the problem can be described in terms of the Reynolds, Richardson, and Peclet numbers, given by $Re = Ud/v$, $Ri = gd\beta\delta\theta/U^2$, and $Pe = Ud/\kappa$. In this calculation, the Reynolds number is 50, the Peclet number

is 7.5, and the Richardson number is 750. The length scale is taken to be the length of the heated substrate. The initial condition is that of plane Poiseuille flow, with the heater "turned on" at $t = 0$. The boundary conditions are no-slip walls, Poiseuille flow at the inlet, and conditions at the outflow plane are implemented in the manner discussed earlier in this paper.

The calculations are shown in Figs. 3a-d. Initially, plumes rise from the surface of the substrate, are pulled downstream, and breap up into discrete vortical structures.
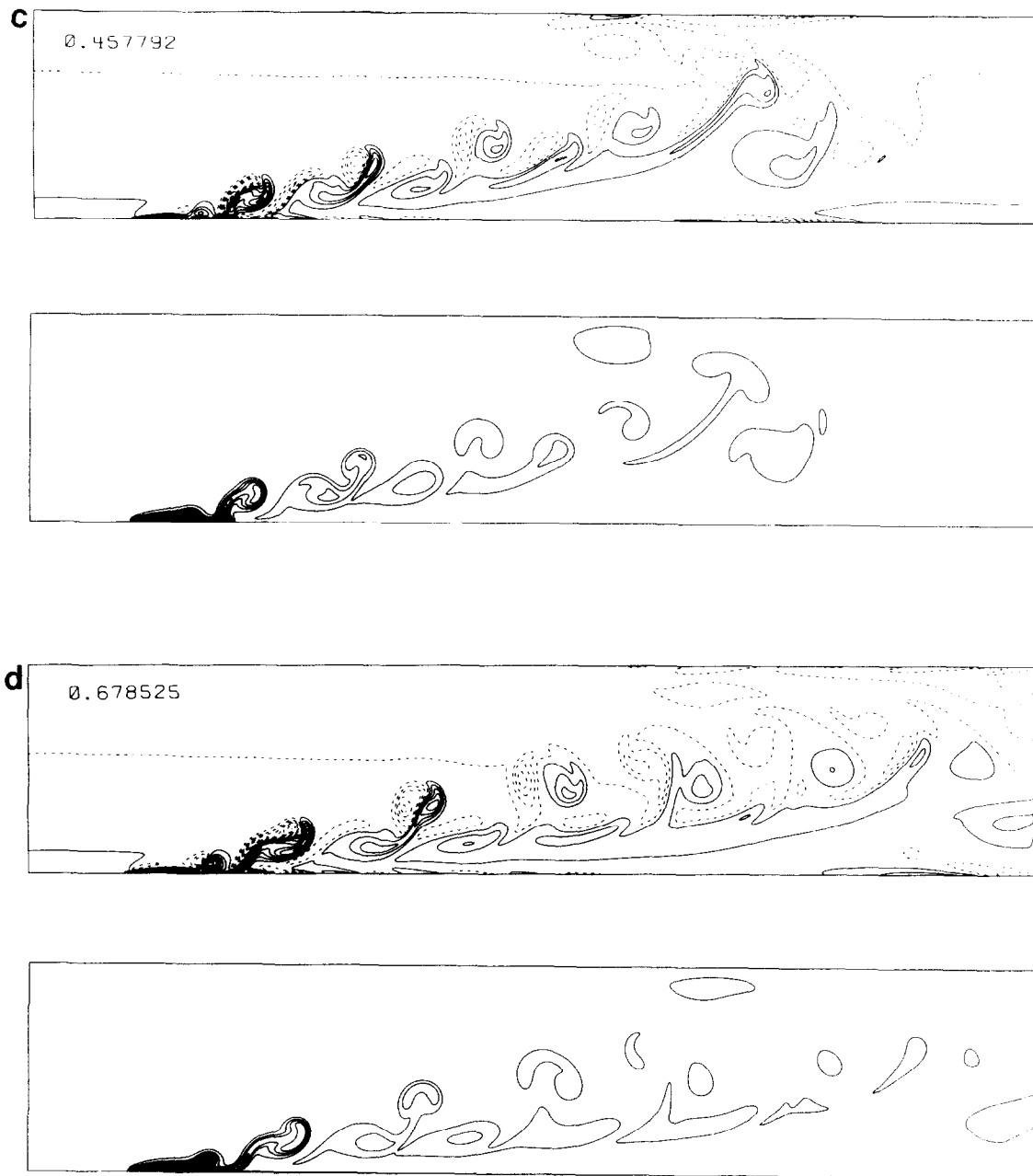
FIG. 3. (c)–(d) Poiseuille flow past a heated strip (continued). Vorticity contours above, temperature contours below. Reynolds number = 50, Peclet number = 7.5, Richardson number = 750.

After the initial perturbation is swept downstream, the flow relaxes to a quasi-steady state in which vortices are shed continually by the substrate, are pulled and stretched downstream, and pass out the outflow boundary. Numerical experiments have shown that the frequency of oscillation is dependent on the Peclet number. Qualitatively similar structures have been observed experimentally [14], where the buoyancy was introduced by the passive injection of small quantities of weak alcohol solution.

4.3. Rayleigh–Taylor Instability

The Rayleigh–Taylor instability, associated with the acceleration of heavy fluid into light under the action of a gravitational field, is generic to a wide range of physical phenomena, and many numerical simulations have been performed [15–17]. The importance of the Rayleigh–Taylor instability in the physics of stratified flows has also led to its wide use as a test case for numerical methods
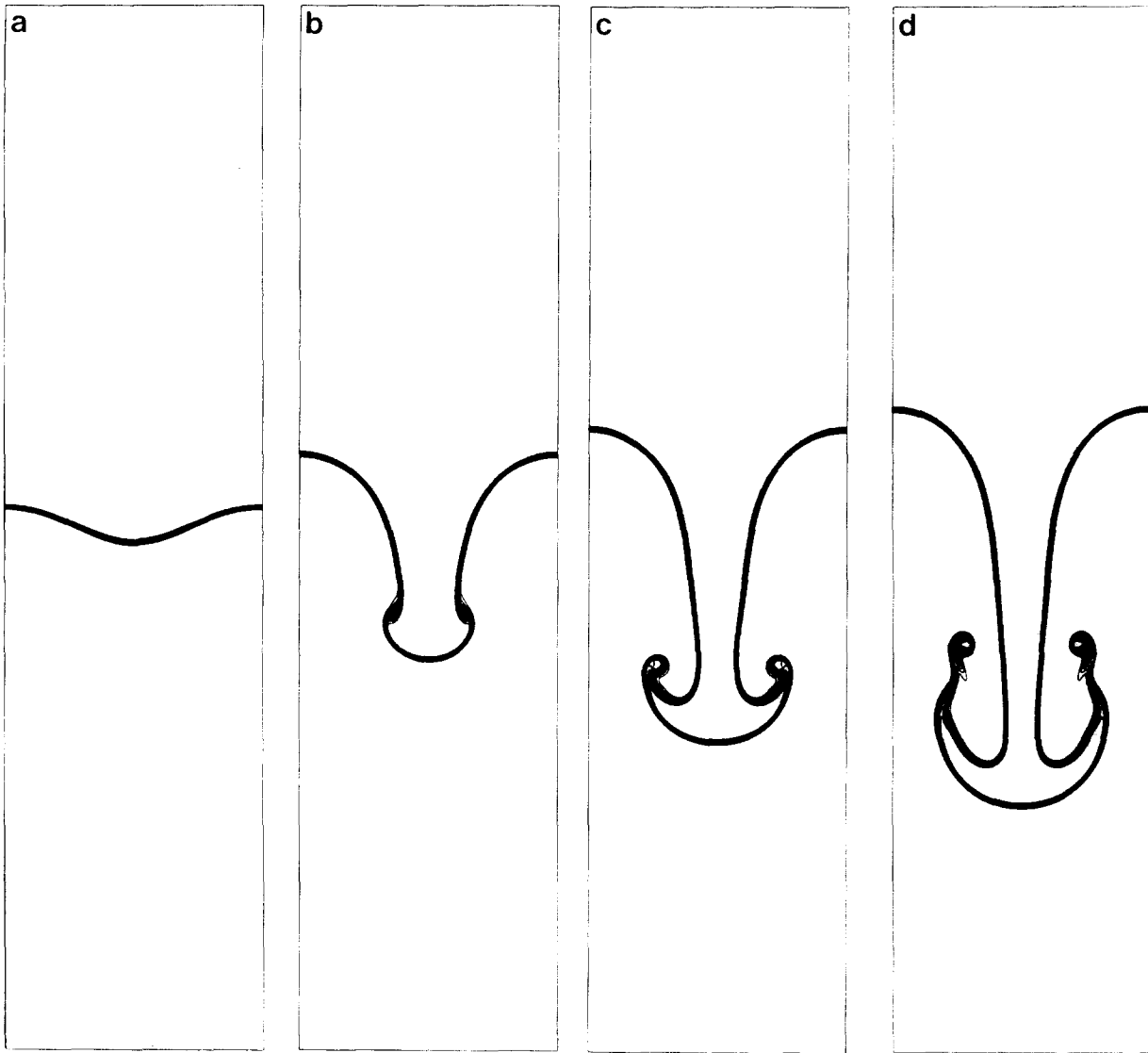
FIG. 4. (a)–(d) Density contours of a Rayleigh–Taylor instability, single-mode initial perturbation, 7:1 density ratio.

applied to such problems. What is most noteworthy about the performance of this method in the context of the Rayleigh–Taylor problem (and, indeed, any sharply stratified flow configuration), is that, in the absence of curvature-dependent physical effects, *no interface tracking scheme is required*; the interface is *captured* in the course of solving the mass conservation equation, using higher-order Godunov methodology. Two calculations are shown: the growth of a single wavelength initial perturbation and the growth of complex initial perturbation, both with periodic boundary conditions horizontally and Dirichlet conditions on the top and bottom.

In the first case, the initial perturbation is given by

$$\eta(x) = 0.01d \cos\left(\frac{2\pi}{d}\right),$$

where d is the width of the computational domain. The interface has been desingularized by a tanh profile of width $0.01d$ to minimize anomalous grid effects. The dimensionless viscosity, $vg^{-0.5}d^{-1.5}$, is 1×10^{-3}, and the density ratio is 7:1, with an Atwood number of 0.875. A uniform 200×800 grid is used. Figures 4a–g show density contours. As the heavy fluid penetrates the light fluid, the interface begins to roll up into two counter-rotating vortices with the characteristic mushroom shape. At this high Atwood number, the rollup is not pronounced, but as the heavy fluid continues to fall, a rich structure develops in the interior of the head.

The complex initial perturbation consisted of a superposition of eight waves of arbitrary wavelength,

$$\eta(x) = 0.00125d \sum_{i=1}^{8} \cos\left(\frac{\lambda_i \pi}{d}\right),$$
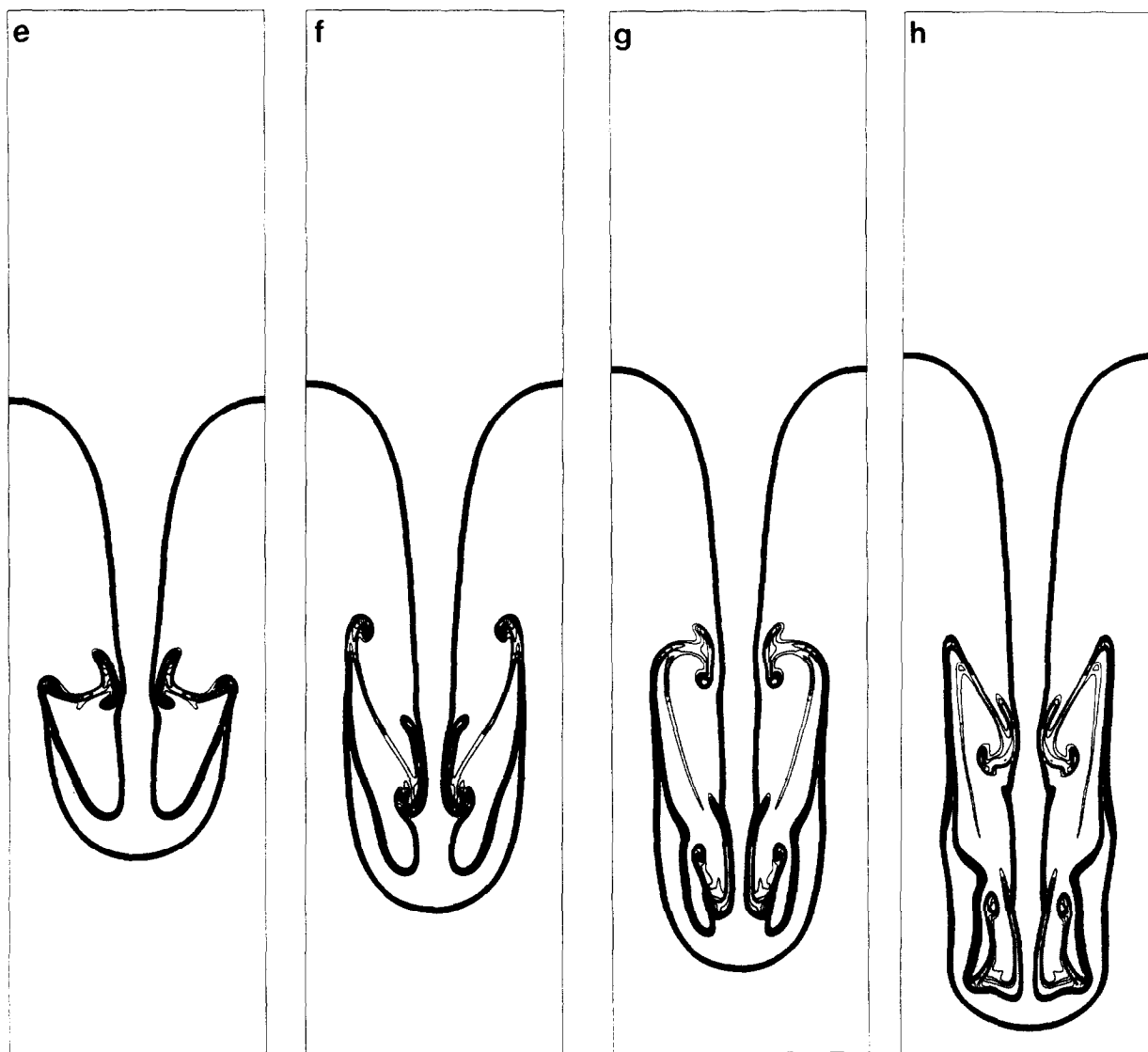
FIG. 4. (e)–(h) Density contours of a Rayleigh–Taylor instability, single-mode initial perturbation (continued), 7:1 density ratio.

where $\lambda = (4, 14, 23, 28, 33, 42, 51, 59)$. The interface has been desingularized as for the single mode case and the viscosity and density ratio are the same. A uniform 250×500 grid is used. Figures 5a–d shows density contours for this case. As Tryggvason has observed in an inviscid, Boussinesq calculation [17], the waves grow almost independently of one another at early times and then begin to interact strongly. Vortex dipoles with length scales much larger than that of any of the initial perturbations are formed and, in some cases, are ejected from the well-mixed region.

4.4. Interaction of a Vortex Ring with a Density Interface

When a vortex ring collides with a density interface, the dynamics are characterized by the interaction of baroclini-

cally generated vorticity with the already existing vorticity field. Examples where this situation can be found are the interaction of a ship or submarine wake with a thermocline and the collision of a buoyant thermal with a temperature inversion. The interaction between vortices and a free surface, which corresponds to the case where the density jump is very large, has been studied fairly extensively, both experimentally [18] and computationally [19–22]. Experiments and numerical studies (the latter in the inviscid, Boussinesq limit) have also been performed for the more general case of vortex pairs and rings interacting with density interfaces [23].

In this example, we calculate the evolution of the vorticity and density fields as a relatively weak axisymmetric vortex ring rising through a viscous, incompressible fluid interacts with a sharp density interface. The Reynolds number (Γ/ν)
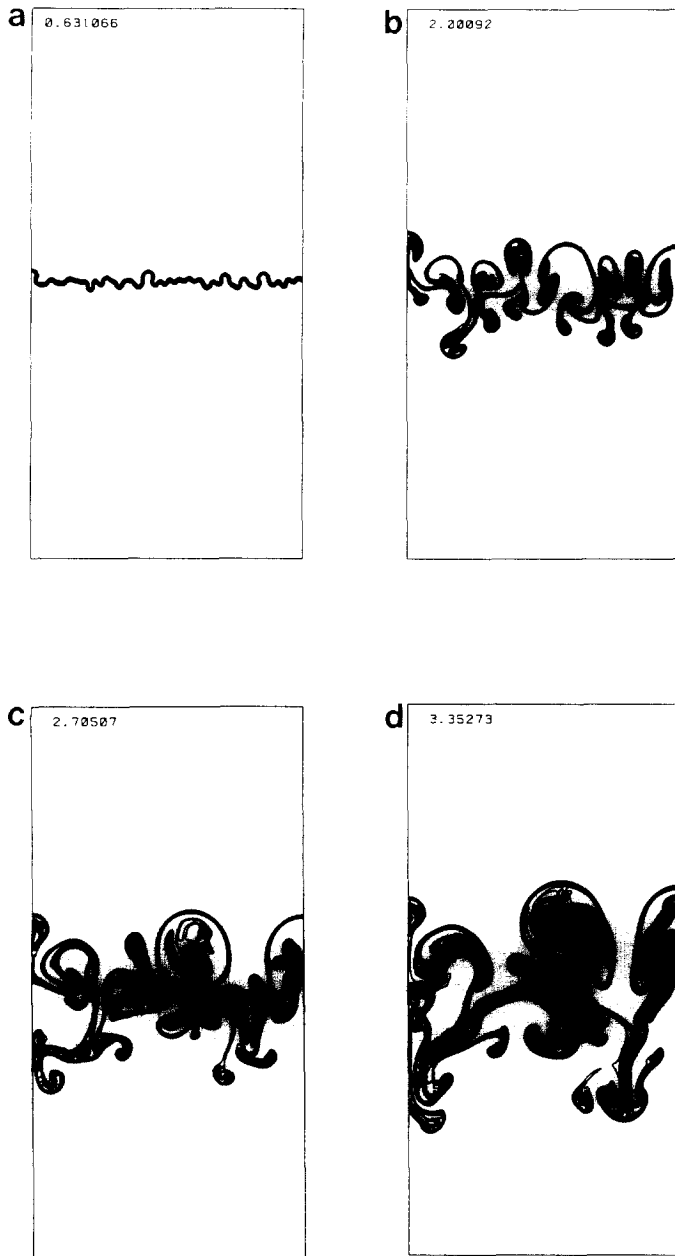
FIG. 5. (a)–(d) Density contours of a Rayleigh–Taylor instability, complex initial perturbation, 7:1 density ratio.

used to initialize the vorticity distribution in the core, and the ratio of core diameter to ring diameter is 0.16. A 250 × 500 grid is used in the calculation. The results are shown in Fig. 6. Vorticity contours are shown on the left and density contours on the right.

Initially, the vortex ring was placed 1.5 diameters below the horizontal interface. It rises under self-advection and the interface deforms, generating baroclinic vorticity along itself. As the vortex becomes closer to the interface, the baroclinically generated vorticity and the already existing vorticity in the ring begin to interact. The ring appears to peel the countersign vorticity from the interface, wrapping it around itself and injecting it back into the heavy fluid below. In the course of doing so, it is almost completely annihilated, and the interface begins to collapse back upon itself. The flow is now quite complex. The main features are the jet penetrating downward into the heavy fluid, and the waves on the interface generated by the collapse of the bubble.

5. CONCLUSION

We have presented a generalization of a second-order projection method for the incompressible Navier–Stokes equations to finite amplitude variable density flows. The use of higher-order Godunov methodology for the nonlinear advection terms in the Navier–Stokes equations provides resolution that permits close study of the fine vortical structure that is characteristic of such flows. Additionally, robust treatment of advection in the mass conservation equation precludes the necessity of coupling a front-tracking algorithm to the solution of the fluid dynamic equations (if properties that depend on interfacial curvature are taken to be small). The method has been shown to be second-order in space and time, and examples have been presented that demonstrate its wide range of applicability. Ongoing and future work include coupling this technology with adaptive mesh refinement [24], so that resolution will be placed in the computational domain only where it is demanded by the evolving flow structure, and developing a front-tracking algorithm to account for curvature-dependent interfacial effects. By combining the basic integration methodology described in this paper with these types of adaptive methodologies, we will be able to perform computations in three dimensions that are comparable in resolution to the results presented here.
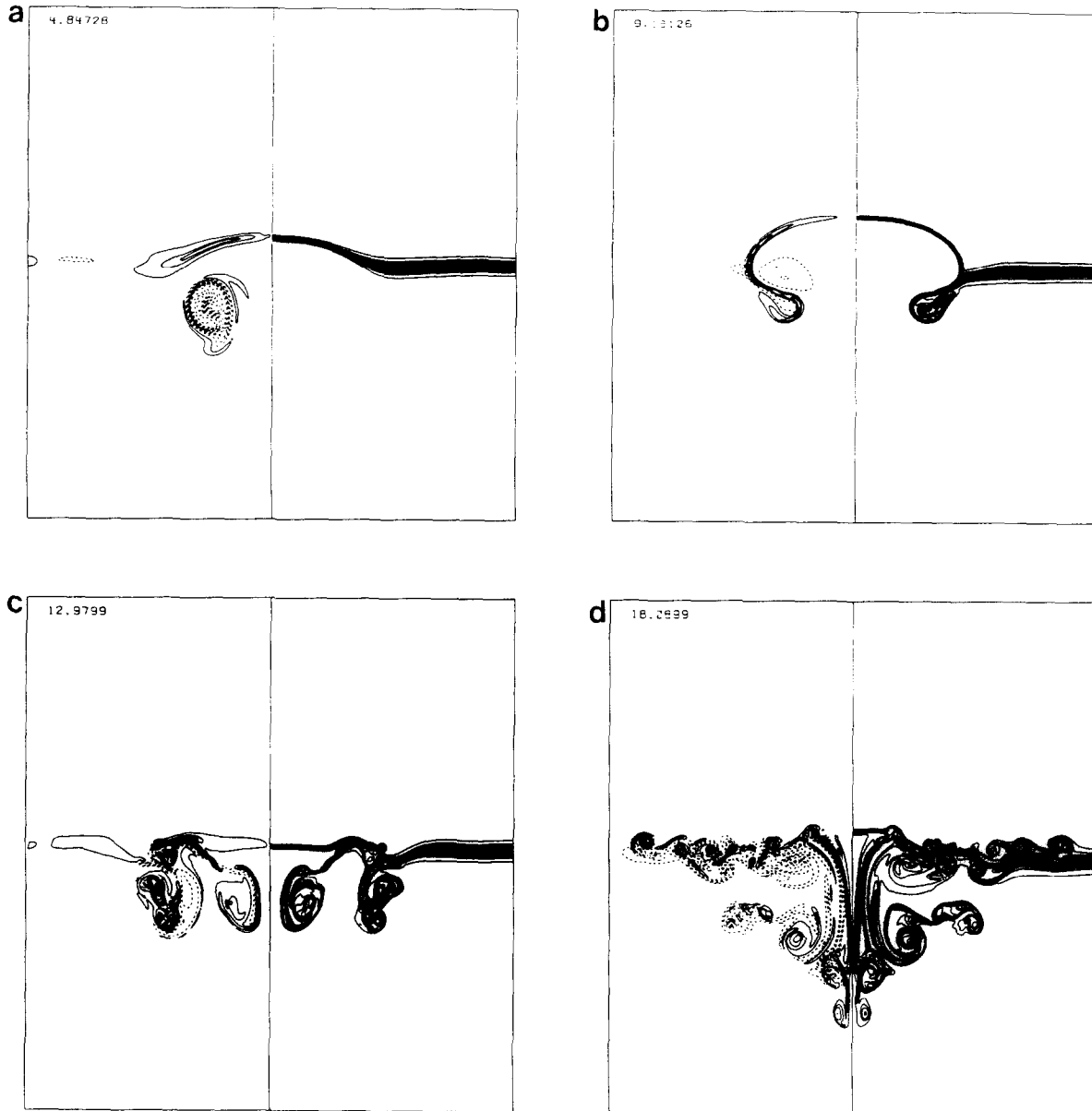
is 3750, the inverse Froude number $(a^3 g/\Gamma^2)$ is 52.7, the Atwood number if 0.8, with a 5:1 density ratio and a stable stratification. Here, Γ is the strenth of the vortex ring, v is the kinematic viscosity, a is the initial diameter of the ring, and g is the acceleration due to gravity. An Oseen model is

FIG. 6. (a)–(d) Interaction of an axisymmetric vortex ring with a density interface, 5:1 density ratio, Reynolds number = 3750, inverse Froude number = 52.7.

REFERENCES

1. J. B. Bell, P. Colella, and H. Glaz, *J. Comput. Phys.* **85**, 257 (1989).

2. A. J. Chorin, *Math. Comp.* **23**, 341 (1969).

3. A. B. Stephens, J. B. Bell, J. M. Solomon, and L. B. Hackerman, *J. Comput. Phys.* **53**, 152 (1984).

4. J. M. Solomon and W. G. Szymczak, "Finite Difference Solutions for the Incompressible Navier–Stokes Equations Using Galerkin Techniques," Fifth IMACS International Symposium on Computer Methods for Partial Differential Equations, Lehigh University, June 19–21, 1984.

5. P. Colella, *J. Comput. Phys.* **87**, 171 (1990).

6. J. B. Bell, J. M. Solomon, and W. G. Szymczak, "A Second-Order Projection Method for the Incompressible Navier Stokes Equations on Quadrilateral Grids," AIAA 9th Computational Fluids Dynamics Conference, Buffalo, NY, June 14–16, 1989.

7. M. Fortin, "Numerical Solutions of the Steady State Navier–Stokes Equations," in *Numerical Methods in Fluid Dynamics*, edited J. J. Smolderen, AGARD-LS-48, 1972.

8. S. Chandrasekhar, *Hydrodynamic and Hydromagnetic Stability* (Clarendon, London/New York, 1961).

9. R. S. Scorer, *J. Fluid Mech.* **2**, 583 (1957).

10. J. S. Turner, *Buoyancy Effects in Fluids* (Cambridge Univ. Press, London/New York, 1973).

11. T. Asaeda and K. Watanabe, *Phys. Fluids A* **5**, 861 (1989).

12. C. R. Anderson, *J. Comput. Phys.* **61**, 417 (1985).

13. D. L. Marcus and J. B. Bell, *J. Fluid. Mech.*, submitted.

14. J. A. C. Humphrey and D. L. Marcus, *Exp. Fluids* **5**, 235 (1987).

15. F. H. Harlow and J. E. Welch, *Phys. Fluids* **8**, 2182 (1965).

16. B. J. Daly, *Phys. Fluids* **10**, 297 (1967).

17. G. Tryggvason, *J. Comput. Phys.* **75**, 253 (1988).

18. T. Sarpkaya, in *16th Symposium on Naval Hydrodynamics* (Nat. Acad. Sci., Washington, DC, 1986). p. 38.

19. W. W. Willmarth, G. Tryggvason, A. Hirsa, and D. Yu, *Phys. Fluids A* **1**, 170 (1989).

20. D. L. Marcus and S. A. Berger, *Phys. Fluids A* **1** (12), 1988 (1989).

21. T. Sarpkaya, J. Elnitsky II, and R. E. Leeker, Jr., in *17th Symposium on Naval Hydrodynamics* (Nat. Acad. Sci., Washington, DC, 1989), p. 53.

22. J. Telste, *J. Fluid Mech.* **201**, 259 (1989).

23. W. J. A. Dahm, C. M. Scheil, and G. Tryggvason, *J. Fluid Mech.* **205**, 1 (1989).

24. M. J. Berger and P. Colella, *J. Comput. Phys.* **82**, 64 (1989).